

ADVANCED ELECTRONIC MATERIALS

Supporting Information

for *Adv. Electron. Mater.*, DOI: 10.1002/aelm.201700377

Nanoimaging of Electronic Heterogeneity in Bi₂Se₃ and Sb₂Te₃ Nanocrystals

Xiaowei Lu, Omar Khatib, Xutao Du, Jiahua Duan, Wei Wei, Xianli Liu, Hans A. Bechtel, Fausto D'Apuzzo, Mingtao Yan, Alexander Buyanin, Qiang Fu, Jianing Chen, Miquel Salmeron, Jie Zeng, Markus B. Raschke,* Peng Jiang,* and Xinhe Bao**

Supporting Information

Nano-imaging of electronic heterogeneity in Bi₂Se₃ and Sb₂Te₃ nanocrystals

Xiaowei Lu†, Omar Khatib†, Xutao Du†, Jiahua Duan, Wei Wei, Xianli Liu, Hans A. Bechtel, Fausto D'Apuzzo, Mingtao Yan, Alexander Buyanin, Qiang Fu, Jianing Chen, Miquel Salmeron, Jie Zeng, Markus B. Raschke*, Peng Jiang*, Xinhe Bao**

†These authors contributed equally to this work.

In this document we provide additional nano-imaging and -spectroscopy data for Bi₂Se₃ and Sb₂Te₃ nanocrystals grown by polyol and CVD methods, respectively, as well as details of model used to simulate the s-SNOM response.

s-SNOM nano-imaging and structural characterization:

In s-SNOM, AFM topography is collected simultaneously with the IR near-field amplitude image. Figure S1 shows a large area ($15 \times 15 \mu\text{m}^2$) scan of a series of Bi₂Se₃ nanocrystals, with AFM topography (Figure S1a) and corresponding s-SNOM amplitude (Figure S1b) obtained at a laser illumination frequency of 977 cm^{-1} . The behavior of these nano-optical patterns is typically rotationally symmetric alternating bright and dark regions, with either a bright or dark core depending primarily on the thickness of the nanocrystal.

The s-SNOM patterns further exhibit a spectral dependence, as shown in Figure S2. For Bi₂Se₃ nanocrystals on SiO₂/Si, s-SNOM contrast relative to the substrate varies significantly as the laser illumination wavelength is scanned through the surface phonon resonance ($\sim 1108 \text{ cm}^{-1}$) of SiO₂, most clearly evident in Figure S2d. Interestingly, the contrast pattern within the nanocrystal is inverted at higher frequencies (Figure S2e,f), with respect to the bright and dark regions, compared to frequencies below the substrate phonon resonance (Figure S2b,c).

To complement the frequency-dependent behavior of the s-SNOM response in monochromatic nano-imaging we performed ultrabroadband nano-spectroscopic synchrotron infrared nano-spectroscopy (SINS). The nature of the symmetric patterns reflecting the crystal symmetry exhibits many similarities to what is attributed to interference from near-field coupled surface waves in materials that host surface plasmon or phonon polariton modes. However, our SINS results (Figure 2 in main text) do not indicate the presence of such resonances in Bi_2Se_3 , as we do not observe any discernible dispersion, and only register an overall signal enhancement that mimics the spatial dependence seen in monochromatic imaging experiments.

On the other hand, such symmetric contrast variation in s-SNOM could arise with the excitation of surface phonon polaritons (SPhPs) waves not in the sample materials itself, but in the substrate. Such surface waves have been observed with s-SNOM in systems such as $\text{SiC}^{[1]}$ and $\text{h-BN}^{[2]}$ and more recently with phase change materials on quartz.^[3] This latter work closely relates to our material systems, where a polaronic resonant substrate is covered by a dielectric spacer consisting of related chalcogen and pnictogen compounds (Bi, Sb, Te, etc). However, in such systems, SPhPs are only expected to be excited within the reststrahlen band of the substrate. For quartz, this is a very narrow frequency region from $\sim 1070\text{--}1230\text{ cm}^{-1}$. As evident in our s-SNOM images, as well as the broadband SINS measurements, the symmetric nano-optical patterns exist at frequencies well outside this energy range. Further, the dielectric response of amorphous SiO_2 is much weaker than crystalline quartz, precluding polariton modes at the interface with high index materials such as Bi_2Se_3 and Sb_2Te_3 .

Further, Bi_2Se_3 nanocrystal samples were also deposited onto a bare Si surface where the oxide was etched off by HF aqueous solution. The resulting IR nano-images, as shown in Figure S3, demonstrate the same s-SNOM behavior seen in nanocrystals on SiO_2/Si . The s-SNOM contrast

in Figure S3b appears weaker due to the significantly enhanced signal of the conducting Si substrate, as compared to insulating SiO₂ except when on resonance with the SiO₂ phonon (Figure S2d). These findings thus exclude the influence of the substrate phonon on the nanocrystal s-SNOM response observed.

Fundamentally, in fact, plasmonic excitations in Bi₂Se₃ and related TIs are expected to have very low energy in the THz or far-IR, outside of our experimental range.^[4] On the other hand, recent electron energy loss spectroscopy work indicates the presence of a collective excitation in Bi₂Se₃ near 100 meV (806 cm⁻¹) with flat dispersion, not due to the 2D Dirac surface states, but instead related to the surface plasmon mode from the bulk carriers.^[5] We therefore cannot explicitly rule out that related excitations at least contribute partially to the optical patterns we observed below 1000 cm⁻¹. However, from the combination of s-SNOM with other elemental probes in this work detailed in the main text and below, we believe instead that such signal enhancement at lower energies is due to an increase in free carrier Drude absorption in areas with higher defect density or vacancies sustained during growth.

Multiple techniques were used to characterize the crystal structure and composition of Bi₂Se₃ nanocrystals. TEM image of a hexagonal Sb₂Te₃ nanocrystal used to selected area electron diffraction (SAED) characterizations is shown in Figure S5a. SAED patterns (Figure S5b-e) taken at different positions marked with white circles in Figure S5a present are consistent, i.e., well-defined six-fold symmetric diffraction spots, manifesting the synthesized nanocrystal is high-quality single crystalline.

We then performed EDX to analyze the distribution of elements. Consistent with the uniform contrast in scanning transmission electron microscopy (STEM; Figure S6a), the corresponding elemental distribution of Se and Bi is homogeneous as well (Figure S6b,c). Compared to EDX,

nano-auger element mapping has higher lateral resolution (~10 nm) and lower detection limit (~0.1 at%), and it has been successfully used to confirm that the grain boundaries, edge and nucleation center of monolayer MoS₂ are S-deficient.^[6] However, in our case, the distribution of Se element revealed by nano-auger is uniform, and no oscillating contrast can be seen (Figure S7b).

High resolution TEM (HRTEM) was employed to image the atomic structure of Bi₂Se₃ nanocrystals. In the HRTEM images (Figure S8a and b taken from the core and edge, respectively, as indicated in the inset), the well-resolved hexagonal lattice fringes with a lattice spacing of 2.0 Å between {110} planes is shown. After fast Fourier transform (FFT), regular hexagonal diffraction patterns (insets, right) indicates a single phase without twin structure. Based on these characterization results and the annealing experiment (Figure 3 in the main text), we believe that there exists a non-uniform distribution of minor point defects (i.e., Se vacancies) that leads to regions with different carrier concentrations. These defects are much lower than the detection limit of traditional techniques, including TEM, EDX and nano-Auger, but have significant impacts on the electronic structure and optical response, and consequently can be probed by IR s-SNOM.

On the other hand, we checked to see if possible Se vacancies can be cured by annealing the nanocrystal under Se atmosphere (Figure S9, Supporting Information). Unfortunately, strong infrared contrast still exists. Thus, we believe that for the polyol-synthesized Bi₂Se₃, Se vacancies cannot be easily eliminated by a post-annealing process.

For comparison and reference to polyol-synthesized Bi₂Se₃, we investigated CVD-grown Bi₂Se₃ (Figure S10, Supporting Information) and Sb₂Te₃ nanocrystals. The infrared optical contrast of CVD-grown Bi₂Se₃ nanocrystals is quite uniform. As for Sb₂Te₃ nanocrystals, we observed

similar nano-optical behavior in IR s-SNOM imaging experiments (Figure 4 in main text). We perform a similar broadband IR nano-spectroscopic characterization for an Sb₂Te₃ nanocrystal on mica, as shown in Figure S11. Similar to Bi₂Se₃, we observe a strongly spatially-dependent s-SNOM response that exhibits a rather weak frequency dependence (Figure S11b-d), with the most dominant spectral feature emerging from the mica substrate phonon, similar to the Bi₂Se₃ nanocrystals on SiO₂. While a slight dispersion is hinted in the nano-spectroscopy line scan (Figure S11c), the signal-to-noise ratio in SINS is too low to clearly discern these subtle features. We therefore perform complementary spectroscopic s-SNOM imaging using a femtosecond tunable mid-IR laser source (A.P.E. GmbH), providing higher spectral irradiance at reduced spectral bandwidth. The resulting contrast in s-SNOM images (Figure S11g) is much more pronounced. With the laser tuned near the peak in the spectral s-SNOM response (see Au reference spectrum in Figure S11i), and with a spectral bandwidth of $\sim 200\text{--}250\text{ cm}^{-1}$, a spectroscopic line scan resolves a strong spatial dependence with a relatively flat frequency response (Figure S11h), suggesting again a variation in carrier concentration instead of a plasmon or phonon polaritonic effect as responsible for the contrast.

s-SNOM model:

As described in the main text, to simulate the nanocrystal s-SNOM response we employ the point dipole model,^[7] where the near-field interaction is described by a coupled tip-sample effective polarizability:

$$\alpha_{eff} = \alpha \left(1 + \frac{\alpha\beta}{16\pi(a+z)^3} \right)^{-1}. \quad (1)$$

Here, z is the height from the sample surface, a is the tip radius, $\alpha = 4\pi a^3 \frac{\epsilon_{Tip} - 1}{\epsilon_{Tip} + 2}$ is the tip

polarizability, and $\beta(\omega)$ incorporates the sample response via $\beta(\omega) = \frac{\varepsilon_{Sample}-1}{\varepsilon_{Sample}+1}$. This simple

formalism must be modified to account for the thin nanocrystal in the form of an effective two-layer system. Following a prescription described in detail elsewhere,^[8-11] we can use an effective dielectric response of the sample that includes the thin surface layer. The near-field Fresnel equations for p-polarized light at an interface are written generally as:

$$r_p(\mathbf{q}, \omega) = \frac{\varepsilon_1 k_0^Z - \varepsilon_0 k_1^Z}{\varepsilon_1 k_0^Z + \varepsilon_0 k_1^Z}, \quad k_i^Z = \sqrt{\varepsilon_i \frac{\omega^2}{c^2} - q^2}. \quad (2)$$

where k_i^Z and q are the out-of-plane and in-plane components of the wavevector, respectively. An important component of s-SNOM is the significant contribution from evanescent waves scattered by the tip, with a distribution of near-field momenta⁸ peaked at $q \sim 1/a \approx 3.3 \times 10^5 \text{ cm}^{-1}$. Consequently, for a bulk material the near-field Fresnel reflection at high q gives $k_i^Z \rightarrow iq$, and $r_p(\mathbf{q}, \omega) \approx \beta(\omega) = \frac{\varepsilon-1}{\varepsilon+1}$, and the simple dipole model is recovered. To include the thin

nanocrystal in our model, we use the point dipole model described by Equation 1, but using $\beta(\omega) = \frac{\varepsilon'(\omega)-1}{\varepsilon'(\omega)+1}$, where:^[9]

$$\varepsilon'(\omega) = \varepsilon_1 \frac{\varepsilon_2 + \varepsilon_1 \tanh qd}{\varepsilon_1 + \varepsilon_2 \tanh qd}. \quad (3)$$

Here, ε_1 and ε_2 are the dielectric functions of the first and second layer, respectively, d is the top layer thickness, and q is the near-field momentum. This momentum q adds a degree of complication to accurately describe the interaction between the AFM tip and a multilayer sample geometry, as we discuss below.

For the nanocrystal dielectric function, we use the simple Drude model to describe the Bi_2Se_3 response (Figure S4b) where our adjustable parameter is the carrier density. We keep as fixed the dielectric constant^[12] $\varepsilon_\infty = 25$, scattering rate^[13] $1/\tau = 600 \text{ cm}^{-1}$, and effective mass^[14] $m = 0.14 m_e$.

We assume a nanocrystal thickness of 15 nm, which was common in our samples. For the SiO₂ substrate, we assume a Lorentzian oscillator centered at $\omega = 1060 \text{ cm}^{-1}$ (Figure S4a) to match literature values of the complex dielectric function.^[15]

As discussed in the main text, we found good qualitative and semi-quantitative agreement with the SINS experimental results assuming a carrier density in Bi₂Se₃ in the 10^{19} cm^{-3} range. The various curves in Figure S4c show the influence of the choice of near-field momentum in Equation 3, which we keep fixed. The entire s-SNOM response includes a large distribution of q values scattered by the tip,^[8] which must all be taken into account for a truly complete description. For simplicity, however, we may choose a dominant q , often taken to be the peak value at the inverse tip radius. In this case, the s-SNOM amplitude behavior is determined by the free carriers in Bi₂Se₃, and the effect of the strong phonon response in SiO₂ is significantly reduced (dashed red and blue lines in Figure S4c). Conversely, if we assume a much smaller $q \sim 1/10a$, the s-SNOM amplitude as expected more closely resembles the bulk SiO₂ substrate (dotted red and blue lines in Figure S4c). For intermediate fixed q values such as $q \sim 1/5a$, the model results still provide good qualitative agreement with the experimental data (red and blue solid curves in Figure S4c). The inability of this simple dipole formalism using a single fixed q value to accurately incorporate all aspects of the thin conducting surface layer and strongly resonant substrate reflects the fact that a real AFM tip is a tapered, elongated object which affects the depth to which s-SNOM is sensitive. Further, our simplified model overestimates the overall s-SNOM response by a factor of two. However, the differences in strength of the spectral features in the two-layer system relative to the bare substrate is successfully reproduced.

To provide the best fit using our simplified model, we use a near-field momentum q scaled by the far-field Fresnel reflection coefficient (black solid line in Figure S4d), which increases the

contribution of the strong SiO₂ phonon to the multilayer s-SNOM response and better matches the experimental results. Using this weighted q value, Figure 2g in the main text shows the predicted s-SNOM amplitude S_2 for Bi₂Se₃ at a variety of carrier concentrations. It is evident that only carrier densities in the $n \sim 10^{19} \text{ cm}^{-3}$ range demonstrate the same spectroscopic behavior seen in our nanocrystals in Figure 2d. Smaller doping results in an indistinguishable amplitude response, while extremely large carrier concentrations drastically change the frequency-dependence. This is further supported by looking at the predicted Drude reflectivity as a function of doping, shown in Figure S4d, which indicates a doping regime where most of the spectral contrast is below the SiO₂ phonon frequency, as we see in our SINS data and single-frequency IR nano-imaging measurements.

Despite good qualitative agreement between our simple model and the experimental data, we must emphasize that in order to more accurately use s-SNOM as a sensitive quantitative measure of defect-related doping in these TI nanocrystal systems, a proper treatment of the tip-sample interaction is required, such as including the full momentum-dependence and incorporating realistic tip geometries.^[16,17]

References

- [1] N. Ocelic, R. Hillenbrand, *Nat. Mater.* **2004**, *3*, 606.
- [2] S. Dai, Z. Fei, Q. Ma, A. S. Rodin, M. Wagner, A. S. McLeod, M. K. Liu, W. Gannett, W. Regan, K. Watanabe, T. Taniguchi, M. Thiemens, G. Dominguez, A. H. C. Neto, A. Zettl, F. Keilmann, P. Jarillo-Herrero, M. M. Fogler, D. N. Basov, *Science* **2014**, *343*, 1125.
- [3] P. N. Li, X. S. Yang, T. W. W. Mass, J. Hanss, M. Lewin, A. K. U. Michel, M. Wuttig, T. Taubner, *Nat. Mater.* **2016**, *15*, 870.

- [4] P. Di Pietro, M. Ortolani, O. Limaj, A. Di Gaspare, V. Giliberti, F. Giorgianni, M. Brahlek, N. Bansal, N. Koirala, S. Oh, P. Calvani, S. Lupi, *Nat. Nanotechnol.* **2013**, *8*, 556.
- [5] A. Politano, V. M. Silkin, I. A. Nechaev, M. S. Vitiello, L. Viti, Z. S. Aliev, M. B. Babanly, G. Chiarello, P. M. Echenique, E. V. Chulkov, *Phys. Rev. Lett.* **2015**, *115*, 216802.
- [6] W. Bao, N. J. Borys, C. Ko, J. Suh, W. Fan, A. Thron, Y. J. Zhang, A. Buyanin, J. Zhang, S. Cabrini, P. D. Ashby, A. Weber-Bargioni, S. Tongay, S. Aloni, D. F. Ogletree, J. Q. Wu, M. B. Salmeron, P. J. Schuck, *Nat. Commun.* **2015**, *6*, 7993.
- [7] R. Hillenbrand, F. Keilmann, *Phys. Rev. Lett.* **2000**, *85*, 3029.
- [8] Z. Fei, G. O. Andreev, W. Z. Bao, L. F. M. Zhang, A. S. McLeod, C. Wang, M. K. Stewart, Z. Zhao, G. Dominguez, M. Thiemens, M. M. Fogler, M. J. Tauber, A. H. Castro-Neto, C. N. Lau, F. Keilmann, D. N. Basov, *Nano Lett.* **2011**, *11*, 4701.
- [9] L. M. Zhang, G. O. Andreev, Z. Fei, A. S. McLeod, G. Dominguez, M. Thiemens, A. H. Castro-Neto, D. N. Basov, M. M. Fogler, *Phys. Rev. B* **2012**, *85*, 075419.
- [10] J. Aizpurua, T. Taubner, F. J. de Abajo, M. Brehm, R. Hillenbrand, *Opt. Expr.* **2008**, *16*, 1529.
- [11] B. Hauer, A. P. Engelhardt, T. Taubner, *Opt. Expr.* **2012**, *20*, 13173.
- [12] H. Koc, H. Ozisik, E. Deligöz, A. M. Mamedov, E. Ozbay, *J. Mol. Model.* **2014**, *20*, 2180.
- [13] K. W. Post, B. C. Chapler, L. He, X. F. Kou, K. L. Wang, D. N. Basov, *Phys. Rev. B* **2013**, *88*, 075121.
- [14] H. L. Cao, J. F. Tian, I. Miotkowski, T. Shen, J. N. Hu, S. Qiao, Y. P. Chen, *Phys. Rev. Lett.* **2012**, *108*, 216803.
- [15] R. Kitamura, L. Pilon, M. Jonasz, *Appl. Opt.* **2007**, *46*, 8118.

[16] A. S. McLeod, P. Kelly, M. D. Goldflam, Z. Gainsforth, A. J. Westphal, G. Dominguez, M. H. Thiemens, M. M. Fogler, D. N. Basov, *Phys. Rev. B* **2014**, *90*, 085136.

[17] B. Y. Jiang, L. M. Zhang, A. H. Castro Neto, D. N. Basov, M. M. Fogler, *J. Appl. Phys.* **2016**, *119*, 054305.

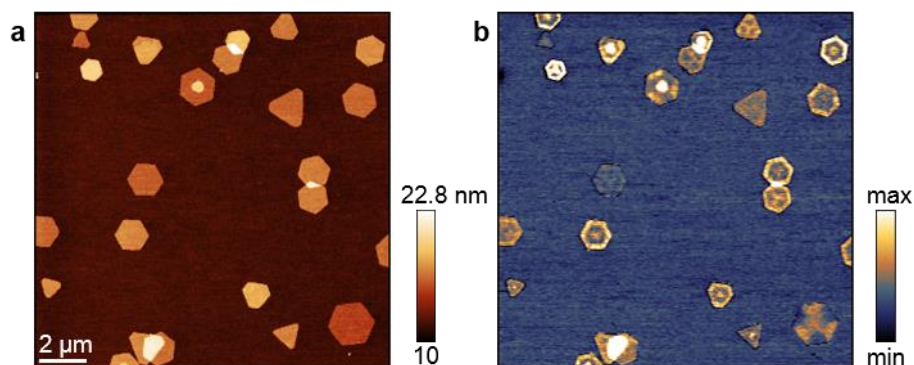


Figure S1. Large-scale s-SNOM scanning of polyol-synthesized Bi_2Se_3 nanocrystals on SiO_2/Si substrate. a-b) Topography (a) and s-SNOM amplitude image (b). Illumination wavelength, 977 cm^{-1} .

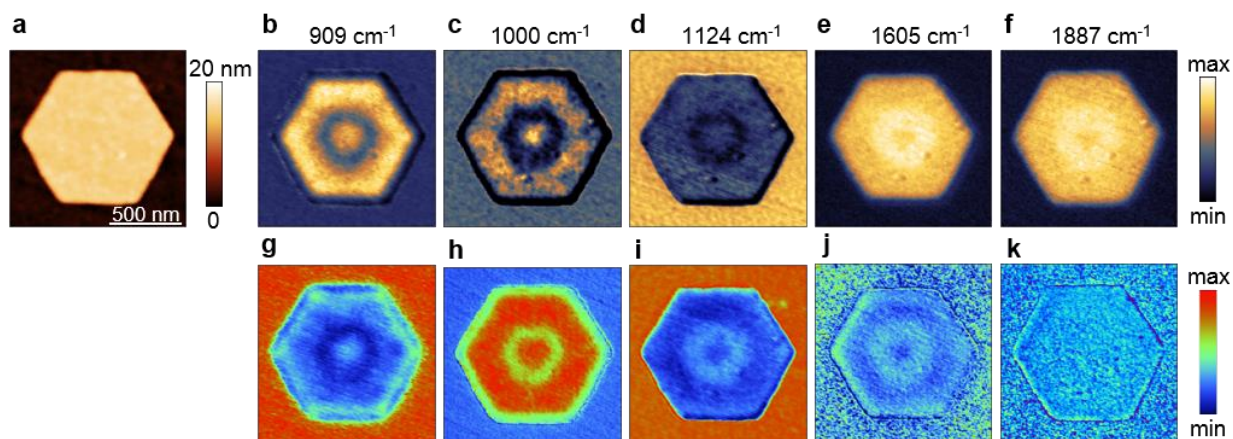


Figure S2. The evolution of near-field contrast observed on polyol-synthesized Bi_2Se_3 nanocrystals with the change of incident wavelength. a) Topography of a Bi_2Se_3 nanocrystal on SiO_2/Si substrate. b-k) The corresponding monochromic s-SNOM amplitude (b-f) and phase (g-k) images taken at five different frequencies, i.e., 909, 1000, 1124, 1605 and 1887 cm^{-1} . The same optical heterogeneity exists in s-SNOM phase images as well.

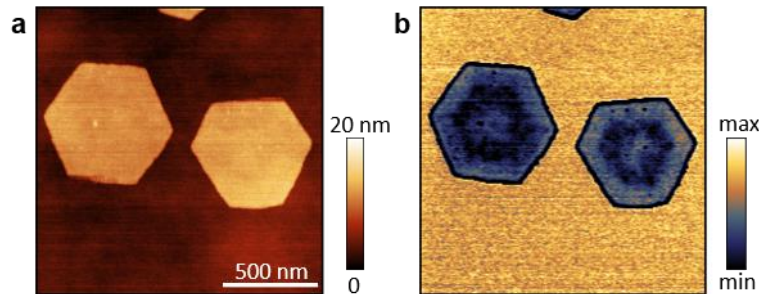


Figure S3. Effects of the type of substrate on the observed optical contrast on polyol-synthesized Bi₂Se₃ nanocrystals. a-b) Topographic (a) and s-SNOM amplitude (b) images of two Bi₂Se₃ nanocrystals on bare Si substrate (native oxide layer was etched). Illumination wavelength, 977 cm⁻¹.

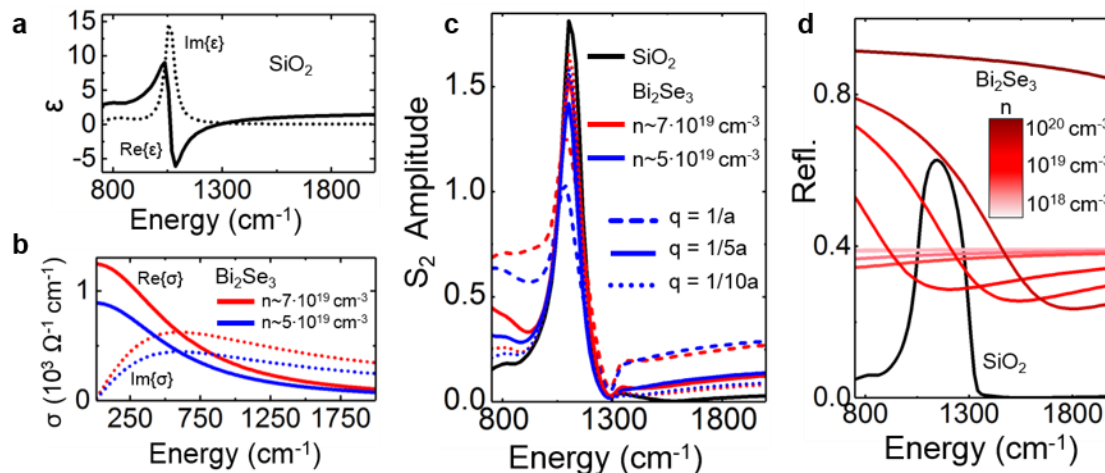


Figure S4. Simulated s-SNOM response of a 15-nm-thick Bi₂Se₃ nanocrystal on SiO₂. a) Dielectric function of SiO₂ substrate. b) Optical conductivity of doped Bi₂Se₃ used in s-SNOM model. c) s-SNOM Amplitude S_2 normalized to Au for bulk SiO₂ (black line) and 15 nm doped Bi₂Se₃ on SiO₂ (blue and red lines) using point dipole model with various fixed in-plane wavevector q . For the largest momenta ($q \sim 1/a$, dashed line), S_2 is dominated by the local Bi₂Se₃ free carrier response, while for smaller momenta ($q < 1/10a$, dotted line) the s-SNOM response more closely resembles the SiO₂ phonon resonance. c-d) Simulated amplitude S_2 (c) and far-field reflectivity (d) for various carrier concentrations of Bi₂Se₃ from 10^{18} to 10^{20} cm^{-3} (red shaded lines) and SiO₂ (black line). Carrier densities in the $n \sim 10^{19} \text{ cm}^{-3}$ range likely give the strongest s-SNOM contrast on the nanocrystals in the frequency range of our nano-imaging and -spectroscopy measurements.

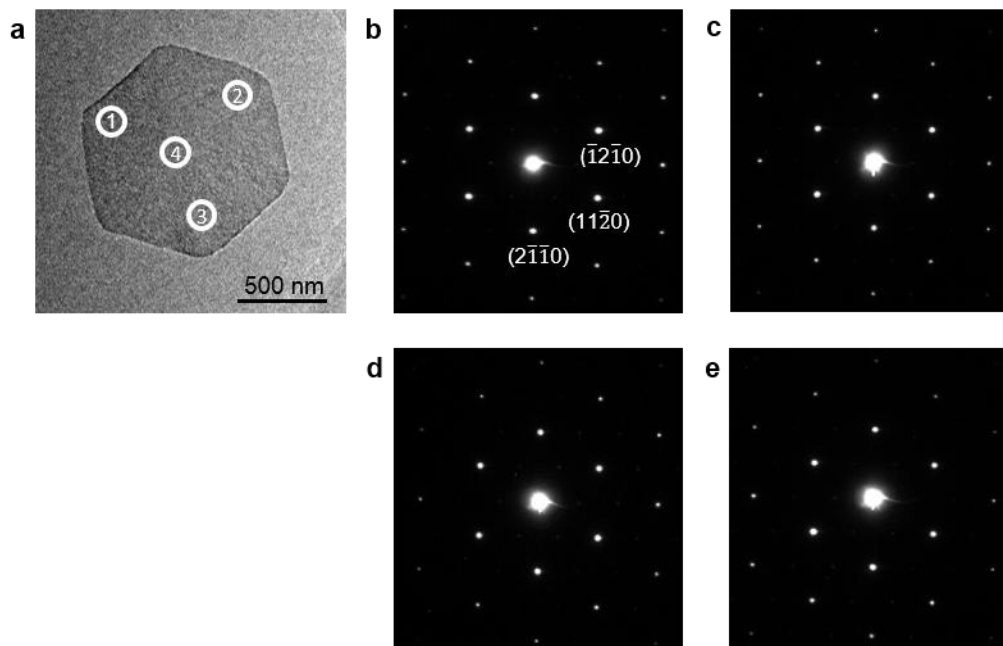


Figure S5. Structural characterization of Bi_2Se_3 nanocrystals. a) TEM image of an individual Bi_2Se_3 nanocrystal. b-e) SAED patterns taken from the different positions labeled in (a) (b-e corresponds to ①-④, respectively).

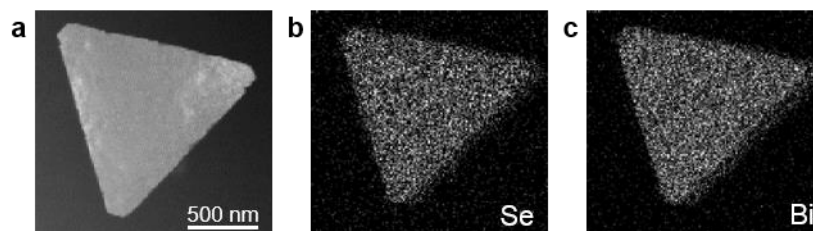


Figure S6. Elementary analysis on Bi_2Se_3 nanocrystals. a) Scanning transmission electron microscopy (STEM) image. b-c) The corresponding EDX elemental mappings of Se (b) and Bi (c).

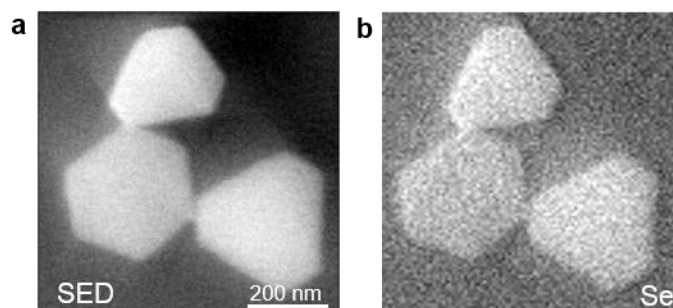


Figure S7. Elementary analysis on Bi_2Se_3 nanocrystals at about 10 nm lateral resolution. a) Secondary electron image of Bi_2Se_3 nanocrystals on Si substrate. b) The corresponding nano-Auger elemental mapping of Se.

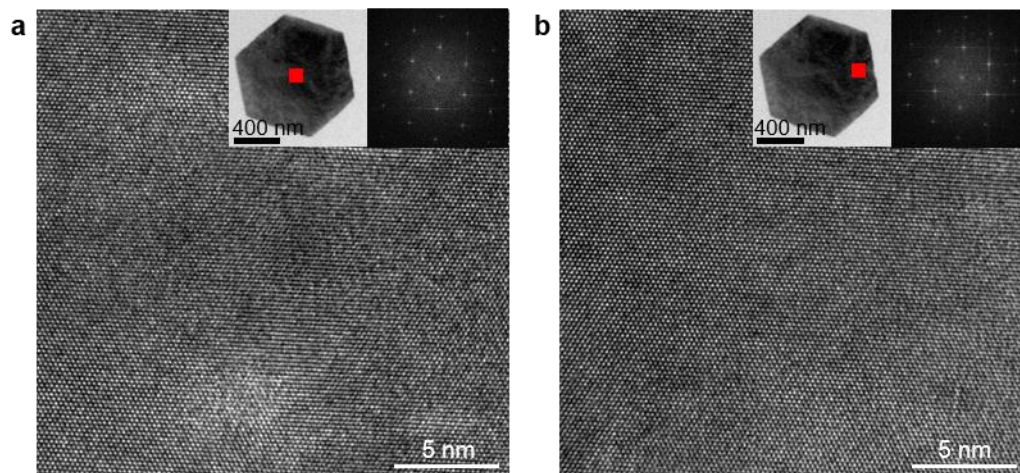


Figure S8. Crystal structure of Bi_2Se_3 nanocrystals. a-b) High resolution TEM (HRTEM) images of a Bi_2Se_3 nanocrystal taken from the core (a) and the edge (b), as labeled in the TEM images (inset, left). The corresponding diffraction patterns obtained by fast Fourier transform (FFT) are also shown (inset, right).

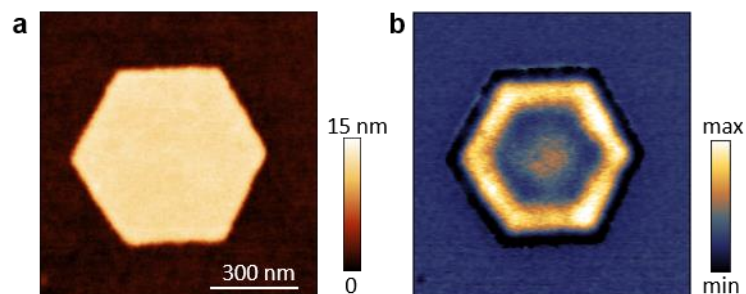


Figure S9. s-SNOM nano-imaging of a polyol-synthesized Bi_2Se_3 nanoplate on SiO_2/Si substrate annealed under Se atmosphere at $300\text{ }^\circ\text{C}$ for 4h. a-b) Topographic (a) and s-SNOM amplitude (b) images. Illumination wavelength, 937 cm^{-1} .

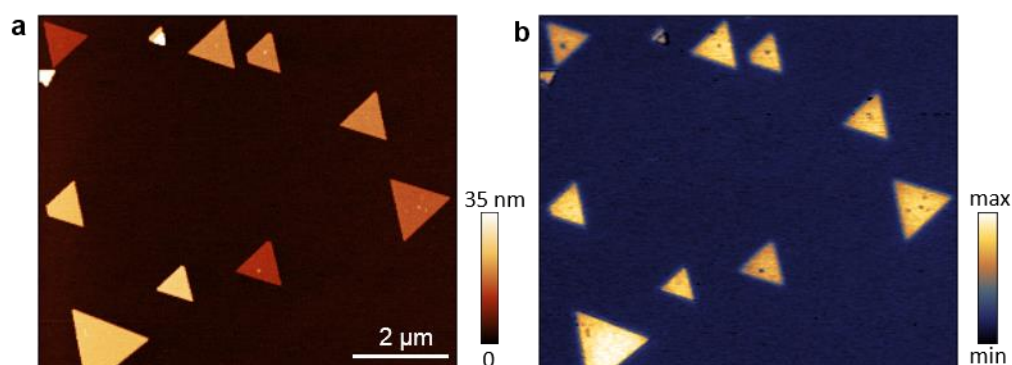


Figure S10. s-SNOM nano-imaging of typical CVD-grown Bi_2Se_3 nanoplates on a mica substrate. a-b) Topographic (a) and s-SNOM amplitude (b) images. Illumination wavelength, 937 cm^{-1} .

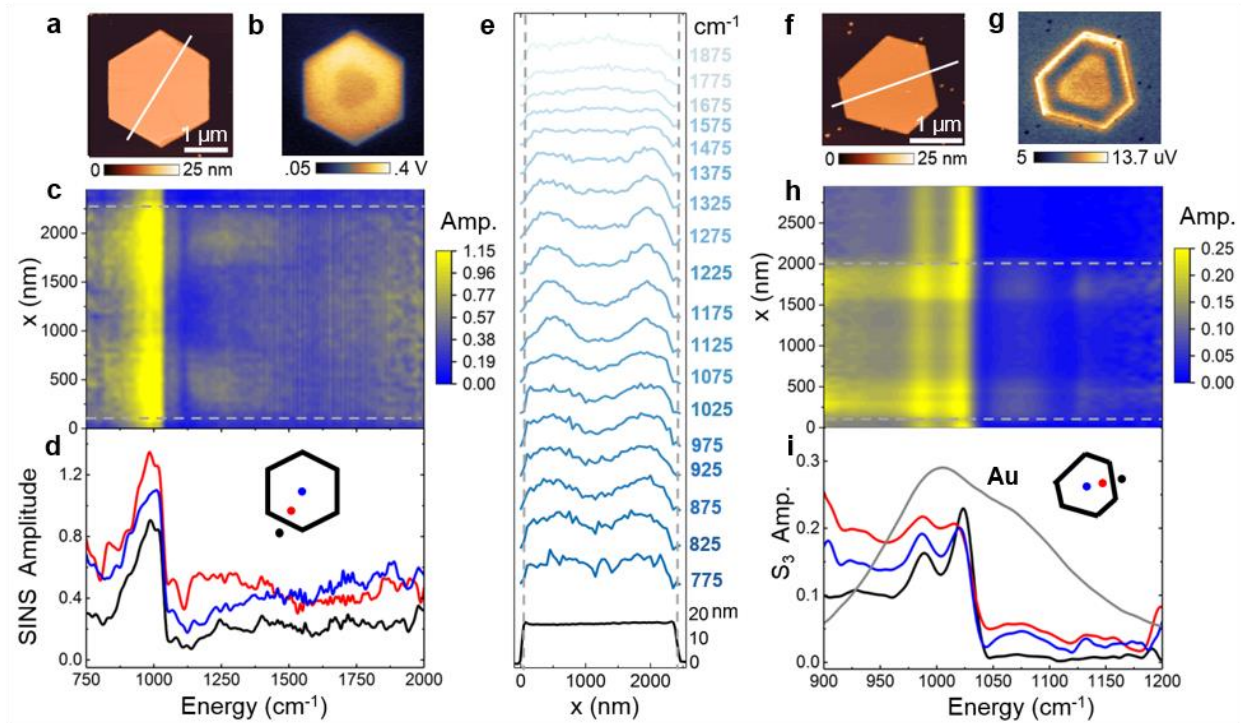


Figure S11. Nanospectroscopy characterization of CVD-grown Sb_2Te_3 nanocrystals on a mica substrate. a-b) AFM topography (a) and spectrally-integrated broadband SINS image (b) of an individual Sb_2Te_3 nanocrystal on mica. c) SINS line scan showing near-field amplitude along the white line in (a). d) Representative SINS spectra, at locations marked by colored circles in inset, showing varying near-field spectral behavior for different positions both on nanocrystal and on substrate. e) Frequency line cuts (shaded blue lines) extracted from (c) at select energies, as indicated, together with the AFM height profile (black line). Grey dashed lines indicate nanocrystal edge. f-i) Independent characterization of the Sb_2Te_3 nanocrystal in Figure 4 in a separate experimental setup. f-g) AFM topography (Anasys, Inc.) (f) and integrated s-SNOM image (g) obtained with narrow-bandwidth ($\sim 250 \text{ cm}^{-1}$) tunable IR laser (A.P.E. GmbH). h-i) Nano-spectroscopic line scan (h) and (i) representative spectra at selected positions indicated in inset, reproducing spectral behavior seen in (c), (d).